NANO EXPRESS

# Silicon and Germanium Nanostructures for Photovoltaic Applications: Ab-Initio Results

**Stefano Ossicini · Michele Amato · Roberto Guerra · Maurizia Palummo · Olivia Pulci**

**Abstract**  Actually, most of the electric energy is being produced by fossil fuels and great is the search for viable alternatives. The most appealing and promising technology is photovoltaics. It will become truly mainstream when its cost will be comparable to other energy sources. One way is to significantly enhance device efficiencies, for example by increasing the number of band gaps in multijunction solar cells or by favoring charge separation in the devices. This can be done by using cells based on nanostructured semiconductors. In this paper, we will present ab-initio results of the structural, electronic and optical properties of (1) silicon and germanium nanoparticles embedded in wide band gap materials and (2) mixed silicon-germanium nanowires. We show that theory can help in understanding the microscopic processes important for devices performances. In particular, we calculated for embedded Si and Ge nanoparticles the dependence of the absorption threshold on size and oxidation, the role of crystallinity and, in some cases, the recombination rates, and we demonstrated that in the case of mixed nanowires, those with a clear interface between Si and Ge show not only a reduced quantum confinement effect but display also a natural geometrical separation between electron and hole.

**Keywords**  Silicon · Germanium · Nanocrystals · Nanowires · Nanophotonics · Photovoltaics

S. Ossicini (✉)
Dipartimento di Scienze e Metodi dell'Ingegneria, Universitá di Modena e Reggio Emilia, via Amendola 2 Pad. Morselli, 42122 Reggio Emilia, Italy
e-mail: ossicini@unimore.it

S. Ossicini · M. Amato · R. Guerra
Centro S3, CNR-Istituto di Nanoscienze, Via Campi 213A, I-41125 Modena, Italy

M. Amato · R. Guerra
Dipartimento di Fisica, Università di Modena e Reggio Emilia, via Campi 213/A, 41125 Modena, Italy

M. Palummo
European Theoretical Spectroscopy Facility (ETSF), CNR-INFM-SMC, Dipartimento di Fisica, Università di Roma, 'Tor Vergata', via della Ricerca Scientifica 1, 00133 Roma, Italy

O. Pulci
European Theoretical Spectroscopy Facility (ETSF), NAST, Dipartimento di Fisica, Università di Roma, 'Tor Vergata', via della Ricerca Scientifica 1, 00133 Roma, Italy

## Introduction

Photovoltaic (PV) energy is experiencing a large interest mainly due to the request for renewable energy sources. It will become mainstream when its costs will be comparable to other sources. At the moment it is too expensive for competitive production. For this reason an intense research activity is of fundamental importance to develop efficient PV devices ensuring a low cost and a low environmental impact. Until now three generations of solar cells have been envisaged [1]. Currently, PV production is 90% first-generation and is based on Si wafers. First generation refers to high quality and hence low-defect single crystal devices and is slowly approaching the limiting efficiencies of about 31% [2] of single-band gap devices. These devices are reliable and durable, but half of the cost is the Si wafer. The second generation of cells make use of cheap semiconductor thin films deposited on substrates to produce low-cost devices of lower efficiency. These thin-film cells account for around 5–6% of the market. For these second-generation devices, the cost of the substrate represents the cost limit and higher efficiency will be needed to maintain

the cost-reduction trend [3]. Third-generation cells use, instead, new technologies to produce high-efficiency devices [4, 5]. They are photo-electrochemical cells based on dye-sensitized nanocrystalline wide bandgap semiconductors [6] or multiple energy threshold devices based on nanocrystalline silicon for the widening of the absorbed solar spectrum, due to the quantum confinement (QC) effect that enlarges the energy gap of the nanostructures, and for the use of excess thermal generation to enhance voltages or carrier collection [7]. Moreover recently also silicon and germanium nanowires have been used and envisaged for PV applications [8–13].

Besides the intense experimental work, devoted to the improvement of the nanostructures growth and characterization techniques and to the realization of the nanodevices, an increasing number of theoretical works, based on empirical and on *ab-initio* approaches, is now available in the literature (see for example Refs. [14–16]). The importance of the theoretical efforts lies not only in the interpretation of experimental results but also in the possibility to predict structural, electronic, optical, and transport properties aimed at the realization of more efficient devices. Important progresses in the description of the electronic properties of Si and Ge nanostructures have been reported, but an exhaustive understanding is still lacking. This is due, on one side to the not obvious transferability of the empirical parameters to low- dimensional systems and on the other side to the deficiency of the *ab-initio* Density Functional Theory (DFT) approach in the correct evaluation of the excitation energies. In fact, due to their reduced dimensionality, the inclusion of many-body (MB) effects in the theoretical description, in the so-called many-body perturbation theory (MBPT), is mandatory for a proper interpretation of the excited state properties. In particular, the quasiparticle structure is a key for the calculation of the electronic gap and to the understanding of charge transport as the inclusion of excitonic effects is really important for a description of the optical properties. In this paper, we apply DFT and MBPT to the calculation of the structural, electronic and optical properties of two classes of systems: pure and alloyed Si/Ge nanocrystals (NCs) embedded in wide band gap $SiO_2$ matrices, and free-standing SiGe mixed nanowires (NWs). These systems have been chosen for their application in photovoltaics, and therefore our results will be discussed with respect to their potentiality. The paper is organized as follows: in section "Ab-initio Methods: DFT and MBPT", we sketched the theoretical methods used in our computations, section "Embedded Si and Ge Nanocrystals" is devoted to the presentation of the results related to the embedded Si and Ge NCs, whereas section "Si/Ge Mixed Nanowires" discusses the outcomes for the mixed SiGe NWs, finally some conclusion is outlined in section "Conclusions".

## Ab-initio Methods: DFT and MBPT

DFT [17, 18] is a single-particle *ab-initio* approach successfully used to calculate the ground-state equilibrium geometry and electronic properties of materials, from bulk to systems of reduced dimensionality like surfaces, nanowires, nanocrystals, nanoparticles.

However, the mean-field description of the MB effects, taken into account in this method, by the so-called exchange-correlation (XC) term, is not enough to describe excited state properties. Even the time-dependent development of this approach, the TDDFT [19, 20], formally appropriate to calculate the optical excitations and the dielectric response of materials, presents problems due to the limited knowledge of the exact form of the XC functional [21, 22]. For these reasons, excited state calculations based on MBPT, performed on top of DFT ones, have become state-of-the-art to obtain a correct description of electronic and optical transition energies. The DFT simulations of our nanostructures are performed using the Quantum Espresso package [23], with a plane-wave (PW) basis set to expand the wavefunctions (WF) and norm-conserving pseudopotentials to describe the electron-ion interaction. The local density approximation (LDA) is used for the XC potential. A repeated cell approach allows to simulate NCs and NWs. A full geometry optimization is performed and, after the equilibrium geometry is reached, a final calculation is made to obtain not only the occupied but also a very high number of unoccupied Kohn-Sham (KS) eigenvalues and eigenvectors ($\varepsilon_{n\mathbf{k}}$, $\psi_{n,\mathbf{k}}$) [24, 25]. In fact, although they cannot be formally identified as the correct quasi-particle (QP) energies and eigenfunctions, they are the starting point to perform MB calculations.

Indeed the second step consists in carrying out GW calculations which give the correct QP electronic gaps. Within the Green functions formalism, the poles of the one-particle propagator correspond to the real QP excitation energies and can be determined as solutions of a QP equation which apparently is very similar to the KS equation but where a non hermitian, non-local, energy dependent self-energy (SE) operator $\Sigma$ [26] replaces the XC potential:

$$\left( -\frac{\nabla_r^2}{2} + V_{\text{ext}}(r) + V_H(r) \right) \psi_{n,\mathbf{k}}^{QP}(r)$$
$$+ \int dr' \Sigma(r, r', \epsilon_{n,\mathbf{k}}^{QP}) \psi_{n,\mathbf{k}}^{QP}(r') = \epsilon_{n,\mathbf{k}}^{QP} \psi_{n,\mathbf{k}}^{QP}(r). \qquad (1)$$

The SE is approximated, here, by the product of the KS Green function $G$ times the screened Coulomb interaction $W$ obtained within the Random Phase Approximation (RPA): $\Sigma = iGW$ [27]. Moreover instead to solve the full

QP equation, its first-order perturbative solution, with respect to $\Sigma - V_{xc}$, is used. In this way the QP energies are obtained:

$$\epsilon_{n,\mathbf{k}}^{QP} = \epsilon_{n,\mathbf{k}}^{LDA} + \frac{1}{1 + \beta_{n,\mathbf{k}}} \langle \psi_{n,\mathbf{k}} | \Sigma_x + \Sigma_c(\epsilon_{n,\mathbf{k}}^{LDA}) - V_{xc}^{LDA} | \psi_{n,\mathbf{k}} \rangle \tag{2}$$

where $\beta_{n\mathbf{k}}$ is the linear coefficient (changed of sign) in the energy expansion of the SE around the KS energies. In eq. 2, $\Sigma_x$ represents the exchange part and $\Sigma_c$ is the correlation part. To determine $\Sigma_c$, a plasmon pole approximation for the inverse dielectric matrix, is assumed [28, 29].

Regarding the ab-initio calculations of the optical properties, by means of the KS or the QP energies and WF it is possible to carry out the calculation of the macroscopic dielectric function of the system at the independent-(quasi) particle level.

$$\epsilon_M(\omega) = \lim_{\mathbf{q} \to 0} \frac{1}{\epsilon_{\mathbf{G}=\mathbf{0}, \mathbf{G}'=0}^{-1}(\mathbf{q}, \omega)}. \tag{3}$$

This formula relies on the fact that, although in an inhomogeneous material the macroscopic field varies with frequency $\omega$ and has a Fourier component of vanishing wave vector, the microscopic field varies with the same frequency but with different wave vectors $q + G$. These microscopic fluctuations induced by the external perturbation are at the origin of the local-field effects (LF) and reflect the spatial anisotropy of the material. In particular for NWs, like other one-dimensional nanostructures [30, 31] it has been demonstrated [32–34] that the classical depolarization is accounted for only if LF are included and it is responsible of the suppression of the low energy absorbtion peaks in the $\perp$ direction, rendering an isolated wire almost transparent in the visible region. A similar anisotropic behavior has been observed in the optical absorption of carbon nanotubes [35], in the photoluminescence spectra of porous Si [36] and in the optical gain in Si elongated nanodots [37].

In any case, at this level of approximation, even if GW corrections are included, still no good agreement with the experimental data is found: in particular one finds optical spectra of Si NWs with peaks at too high energy with respect to the experimental optical data, available, for example, for porous Si samples (see Ref. [32] for more details). In order to describe correctly the optical response, the solution of the Bethe–Salpeter equation (BSE), where the coupled electron-hole (e-h) excitations are included [20, 25], is required. In the Green's functions formalism, the solution of the BSE corresponds to diagonalize the following excitonic problem

$$(\epsilon_{ck} - \epsilon_{vk})A_{cvk}^\lambda + \sum_{c'v'k'} <cvk|W - 2V|c'v'k'> A_{cvk}^\lambda$$
$$= E_\lambda A_{cvk}^\lambda \tag{4}$$

where $(\varepsilon_{ck} - \varepsilon_{vk})$ are the quasi-particle energies obtained within a GW calculation, $W$ is the statically screened Coulomb interaction, $V$ is the bare Coulomb interaction, and $A_{cvk}^\lambda$ are the excitonic amplitudes. In this way the e-h wavefunction, corresponding to the exciton energy $E_\lambda$ is obtained as

$$\psi^\lambda(r_e, r_h) = \sum_{c,v,k} A_{cvk}^\lambda \psi_{c,k}(r_e) \psi_{v,k}^*(r_h). \tag{5}$$

## Embedded Si and Ge Nanocrystals

In this section we present ab-initio results for Si and Ge NCs, pure and alloyed, that are embedded in a $SiO_2$ matrix. The role of crystallinity (symmetry) is investigated by considering both the crystalline (betacristobalite (BC)) and the amorphous phases of the $SiO_2$, while size and interface effects emerge from the comparison between NCs of different diameters. A mixed half-Si/half-Ge NC is additionally introduced in order to explore the effects of alloying. The BC $SiO_2$ is well known to give rise to one of the simplest NC/$SiO_2$ interface because of its diamond-like structure [38]. The crystalline embedded structures have been obtained from a BC cubic matrix by removing all the oxygens included in a cutoff-sphere, whose radius determines the size of the NC. By centering the cutoff-sphere on one Si atom or in an interstitial position it is possible to obtain structures with different symmetries. The pure Ge-NCs and the Si/Ge alloyed NCs are obtained from such structures by replacing all or part of the NC Si-atoms with Ge-atoms. In such initial NC, before the relaxation, the atoms show a bond length of 3.1 Å, larger with respect to that of the Si (Ge) bulk structure, 2.35 Å (2.45 Å). No defects (dangling bonds) are present, and all the O atoms at the NC/$SiO_2$ interface are single bonded with the Si (Ge) atoms of the NC.

To model NCs of increasing size, we enlarge the hosting matrix so that the separation between the NC replicas is still around 1 nm, enough to correctly describe the stress localized around each NC [39–41] and to avoid the overlapping of states belonging to the NC, due to the application of periodic boundary conditions [42].

The optimized structure has been achieved by relaxing the total volume of the cell. The relaxation of all the structures have been performed using the SIESTA code [43, 44] and Troullier–Martins pseudopotentials with nonlinear core corrections. A cutoff of 250 Ry on the electronic density and no additional external pressure or stress were applied. Atomic positions and cell parameters have

been left totally free to move. Following the procedure described above, seven embedded system have been produced: the $Si_{10}$, $Si_{17}$, $Ge_{10}$, and $Ge_{17}$ structures have been obtained from a BC-2x2x2 supercell (192 atoms, supercell volume $V_s = 2.94$ nm$^3$), while for the $Si_{32}$, $Ge_{32}$, and $Si_{16}Ge_{16}$ NCs the larger BC-3x3x3 supercell (648 atoms, supercell volume $V_s = 9.94$ nm$^3$) has been used. Table 1 (upper set) reports some structural characteristics for all the systems enumerated earlier. In all the cases, after the relaxation the silica matrix gets strongly distorted in the proximity of the NC, with Si–O–Si angles lowering from 180 to about 150-170 degree depending on the interface region, and reduces progressively its stress far away from the interface [45]. The difference between the BC lattice constant (7.16 Å) with that of bulk-Si (5.43 Å) and bulk-Ge (5.66 Å) results in a strained NC/SiO$_2$ interface. Therefore, the NC has a strained structure with respect to the bulk value [46–48], and both the NC and the host matrix symmetries are lowered by the relaxation procedure.

Together with the crystalline structure, the complementary case of an amorphous silica (a-SiO$_2$) has been considered. The glass model has been generated using classical molecular dynamics (MD) simulations of quenching from a melt, as described in Ref. [49]. The amorphous a-Si$_{10}$ and a-Si$_{17}$ embedded NCs and their corresponding Ge-based counterparts have been obtained starting from the $Si_{64}O_{128}$ glass (supercell volume $V_s = 2.76$ nm$^3$), while for the a-Si$_{32}$ and a-Ge$_{32}$ NCs the larger $Si_{216}O_{432}$ glass have been used (supercell volume $V_s = 9.13$ nm$^3$). The structural characteristics of the embedded amorphous NCs are reported in Table 1 (lower set). We find that the number of bridge bonds (Si–O–Si or Ge–O–Ge, where Si or Ge are atoms belonging to the NC) increases with the dimension of the NC (three for the largest case and none for the smallest NC) in nice

agreement with other structures obtained by different methods [50, 51]. For each structure we calculated the eigenvalues and eigenfunctions using DFT-LDA and in some cases MBPT [23, 24, 52]. An energy cutoff of 60 Ry on the PW basis has been considered.

## Pure Si Nanocrystals

We resume here results previously obtained for pure Si NCs embedded in SiO$_2$ matrices [24, 53–57]. These results provide not only a good starting point for the comparison between pure Si and pure Ge NCs (see III B) and with alloyed NCs (see III C), but also allow to discuss our results in view of the theoretical methods used (MBPT vs DFT-LDA) and with respect to the technological applications.

As discussed in section "Ab-initio Methods: DFT and MBPT", it is well known that the DFT-LDA severely underestimates the band gaps for semiconductors and insulators. A correction to the fundamental band gap is usually obtained by calculating the QP energies via the GW method [20]. The QP energies, however, are still not sufficient to correctly describe a process in which e-h pairs are created, such as in the optical absorption and luminescence. Their interaction can lead to a dramatic shift of peak positions as well as to distortions of the spectral lineshape. Table 2 shows the highest-occupied-molecular-orbital (HOMO)—lowest-unoccupied-molecular-orbital (LUMO) gap values calculated at the DFT-LDA level for three different Si NC embedded in a crystalline or amorphous SiO$_2$ matrix. These values are compared with the HOMO-LUMO gap values relative to the silica matrices. In Table 3, we report, instead, the results of the MB effects [52] on the DFT gap values, through the inclusion of the GW, GW+BSE and GW+BSE+LF. It should be noted

**Table 1** Structural characteristics of the embedded crystalline (upper set) and amorphous (lower set) NCs: number of NC atoms, number of core atoms (not bonded with oxygens), symmetry (cutoff sphere centered or not on one silicon), number of oxygens bonded to the NC, number of bridge-bonds (see the text), average diameter $d$, supercell volume $V_s$

| Structure | NC atoms | NC-core atoms | Si-centered | Interface-O | Bridge-bonds | $d$ (nm) | $V_s$ (nm$^3$) |
|---|---|---|---|---|---|---|---|
| Si$_{10}$/SiO$_2$ | 10 | 0 | No | 16 | 0 | 0.6 | 2.65 |
| Si$_{17}$/SiO$_2$ | 17 | 5 | Yes | 36 | 0 | 0.8 | 2.61 |
| Si$_{32}$/SiO$_2$ | 32 | 12 | No | 56 | 0 | 1.0 | 8.72 |
| Ge$_{10}$/SiO$_2$ | 10 | 0 | No | 16 | 0 | 0.6 | 2.71 |
| Ge$_{17}$/SiO$_2$ | 17 | 5 | Yes | 36 | 0 | 0.8 | 2.53 |
| Ge$_{32}$/SiO$_2$ | 32 | 12 | No | 56 | 0 | 1.0 | 8.88 |
| Ge$_{16}$Si$_{16}$/SiO$_2$ | 32 | 12 | No | 56 | 0 | 1.0 | 8.77 |
| a-Si$_{10}$/a-SiO$_2$ | 10 | 1 | Yes | 20 | 0 | 0.6 | 2.61 |
| a-Si$_{17}$/a-SiO$_2$ | 17 | 5 | Yes | 33 | 3 | 0.8 | 2.49 |
| a-Si$_{32}$/a-SiO$_2$ | 32 | 7 | No | 45 | 3 | 1.0 | 8.67 |
| a-Ge$_{10}$/a-SiO$_2$ | 10 | 1 | Yes | 20 | 0 | 0.6 | 2.69 |
| a-Ge$_{17}$/a-SiO$_2$ | 17 | 5 | Yes | 33 | 3 | 0.8 | 2.56 |
| a-Ge$_{32}$/a-SiO$_2$ | 32 | 7 | No | 45 | 3 | 1.0 | 8.90 |

**Table 2** DFT-LDA HOMO-LUMO gap values (in eV) for the crystalline and amorphous silica, and for the embedded Si nanocrystals

|             | $SiO_2$ | $Si_{10}/SiO_2$ | $Si_{17}/SiO_2$ | $Si_{32}SiO_2$ |
|-------------|---------|-----------------|-----------------|----------------|
| Crystalline | 5.44    | 1.77            | 2.36            | 2.62           |
| Amorphous   | 5.40    | 1.41            | 1.79            | 1.19           |

**Table 3** Many-body effects on the energy gap values (in eV) for the crystalline and amorphous embedded $Si_{10}$ dots

|             | DFT  | GW   | GW+BSE | GW+BSE+LF |
|-------------|------|------|--------|-----------|
| Crystalline | 1.77 | 3.67 | 1.99   | 2.17      |
| Amorphous   | 1.41 | 3.11 | 1.20   | 1.51      |

that in these last two cases the values are inferred from the calculated absorption spectra.

First, we note that the HOMO-LUMO gap for the crystalline cases seems to increase with the NC size, in opposition to the behavior expected assuming the validity of the QC effect. As discussed in Ref. [53] such deviation from the QC rule can be explained by considering the oxidation degree at the NC/SiO2 interface: for small NC diameters the gap is almost completely determined by the average number of oxygens per interface atom, while QC plays a minor role. Besides, also other effects such as strain, defects, bond types, and so on, contribute to the determination of the fundamental gap, making the system response largely dependent on its specific configuration. Moreover, looking at Table 3 we note that for the $Si_{10}$ and a-$Si_{10}$ embedded NCs the SE (calculated through the GW method) and the e-h Coulomb corrections (calculated through the Bethe–Salpeter equation) more or less exactly cancel out each other (with a total correction to the gap of the order of 0.2 eV) when the LF effects are neglected. Besides we note the presence of large exciton binding energies, of the order of 1.5 eV, similarly to other highly confined Si and Ge systems [32, 58–60]. Furthermore, some our recent calculations (still unpublished) show that the LF effects actually blue-shifts the absorption spectrum of the smallest systems (d < 1 nm), with corrections of the order of few tenths of eV. Instead, for larger NCs no blue-shift is observed. Therefore, while such corrections should be taken into account for a rigorous calculation, we expect that the LF effects will have the same influence on Si and Ge NCs of the same size and geometry, allowing in principle a straightforward comparison between the responses of the two compounds. Besides, Table 3 and previous MB calculations on Si-NCs show absorption results very close to those calculated with DFT-LDA in RPA [24, 55, 61, 62]. In fact these results show that the energy position of the absorption onset is practically not modified by the

inclusion of MB effects. The arguments remarked above justify the choice of DFT-LDA for the results discussed in sections. "Comparison Between Pure Si and Ge Nanocrystals" and "Alloyed Si/Ge Nanocrystals", assuring a good compromise between results accuracy and computational effort.

Concerning the applications we demonstrated [56] that the emission rates follow a trend with the emission energy that is nearly linear for the hydrogenated NCs and nearly cubic for the NCs passivated with OH groups or embedded in $SiO_2$. Moreover, the hydrogenic passivation produces higher optical yields with respect to the hydroxilic one, as also evidenced experimentally. Besides, for the hydroxided NCs the emission is favored for systems with a high O/Si ratio. In particular the analysis of the results for the embedded NCs reveals a clear picture in which the smallest, highly oxidized, crystalline NCs, belong to the class of the most optically-active Si/SiO₂ structures, attaining impressive rates of less than 1 ns, in nice agreement with experimental observations. From the other side, a reduction of five orders of magnitude (10 ms) of the emission rate is achievable by a proper modification of the structural parameters, favoring the conditions for charge-separation processes, thus photovoltaic applications [56]. In the case of strongly interacting systems (i.e. when the separation between the NCs lowers under a certain limit), the overlap of the NCs WF becomes relevant, promoting the tunneling process. Therefore, while for the single Si/SiO₂ heterostructure the e-h pair is confined on the NC, in the case of two (or more) interacting NCs a charge migration from one NC to the neighbor can occur [63]. Evidence of an interaction mechanism operating between NCs has been frequently reported [64–66], sometimes indicated as an active process for optical emission [67], and sometimes even exploited as a probing technique [68]. This interaction has been widely interpreted in terms of a kind of excitonic hopping or migration between NCs, although only more recently the mechanisms for carrier transfer among Si-NCs have been more clearly elucidated [69, 70]. Roughly speaking, the possibility of charge migration reduces the QC effect, possibly leading to the formation of minibands with indirect gaps [63]. It should be noted that, contrary to photonics applications, for PV purposes the indirect nature of the energy bandgap in Si-NCs is advantageous, since the photogenerated e-h pair has a longer lifetime with respect to direct bandgap materials. Therefore, the NC–NC interaction can be considered as an additional parameter (tunable by the NC density) that concurs to the characterization of the system behavior: while the NC-size primarily determines the absorption/emission energy, the interaction level affects the absorption/emission rates. This picture opens to the possibility of creating from one side (high rates) extremely efficient

Si-based emitters [71], and from the other side (low rates) PV devices capable to harvest the full solar energy with high yields. While the role of the NC size has been extensively investigated by many works, as theoretically like as experimentally, the study of the effects of NC–NC interplay is still at an early stage, due to the difficulties encountered.

Comparison Between Pure Si and Ge Nanocrystals

In this section, we compare the responses of the pure Si and Ge NCs at the DFT-LDA level. The density of states (DOS) calculation provides a first insight into the electronic configuration. In Fig. 1, we report the DOS for the crystalline Si and Ge NCs for an energy region focused around the band edge. All the DOS have been normalized following the constraint

$$\int_{-\infty}^{E_F} \mathrm{DOS}(E)\mathrm{d}E = 1, \tag{6}$$

in which $E_F$ is the Fermi energy located half-between the HOMO and the LUMO.

The analysis of Fig. 1 reveals that Ge-NCs present reduced gaps with respect to their Si counterparts. This could be reasonably associated with the reduced band-gap value of bulk-Ge with respect to bulk-Si. The $Ge_{10}$ case is an outlier to this rule, showing a gap slightly larger than the $Si_{10}$ NC. This exception can be justified by considering that such NCs represent a limit case in which all the NC atoms are localized at the interface.

It is noteworthy that the DOS profile arising from conduction states is similar for Si- and Ge-based structures of the same size, while the DOS profile arising from valence states differs for the two species. In particular, in the case

of Ge-NCs the energy region around the valence band edge tends to be densely occupied, while for Si-NCs only few discrete levels appear in that region.

The DOS for the amorphous Si and Ge embedded NCs is reported in Fig. 2. The symmetry breaking deriving from the amorphyzation evidently broadens the energy distribution of the states, consequently reducing the HOMO-LUMO gap. The discussion concerning the gap-reduction for Ge NCs is still valid in the amorphous case, with Ge systems presenting similar or smaller gaps with respect to the equivalent Si counterparts. This effect is particularly evident for the a-$Ge_{32}$ NC in which several states gets localized within the band gap due to the amorphyzation.

The properties of the calculated DOS reflect into the absorption spectra (represented by the imaginary part of the dielectric function calculated in RPA) presented in Fig. 3 for all the pure Si and Ge NCs. We clearly distinguish the absorption features associated to the embedding matrix, for energies above 7 eV, that do not depend on the embedding species nor on the NC size. Instead, for energies lower than 7 eV the absorption curve shows a dramatic sensitivity to the NC configuration. In particular, we observe in this region a broadening of the absorption peaks with the NC size, demonstrating that the interface effects become very important for smaller NCs (i.e. when the proportion of atoms at the interface becomes larger). As expected from the DOS analysis discussed earlier, the amorphyzation tends to produce smoother spectra, as for the low-energy region (NC) like as for high-energy one ($SiO_2$ matrix). Finally, for all the sizes, Ge-NCs present lower absorption thresholds with respect to the Si-NCs, mostly due to the higher occupation of the valence band discussed earlier. In Fig. 4, we report the absorption thresholds, calculated from the absorption spectra, corresponding to the minimum
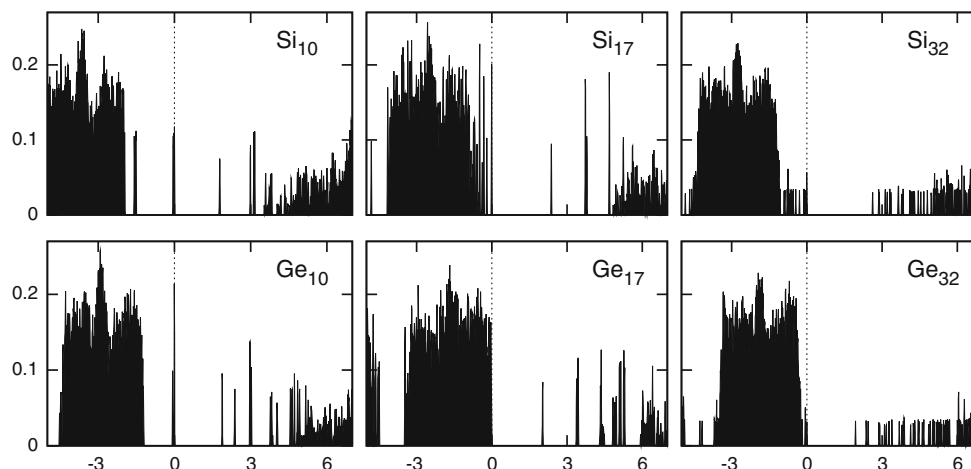


Fig. 1 Normalized DOS for the crystalline pure Si and Ge NCs. Energy units are in eV. The *dotted lines* marks the HOMO state that has been positioned at 0 eV
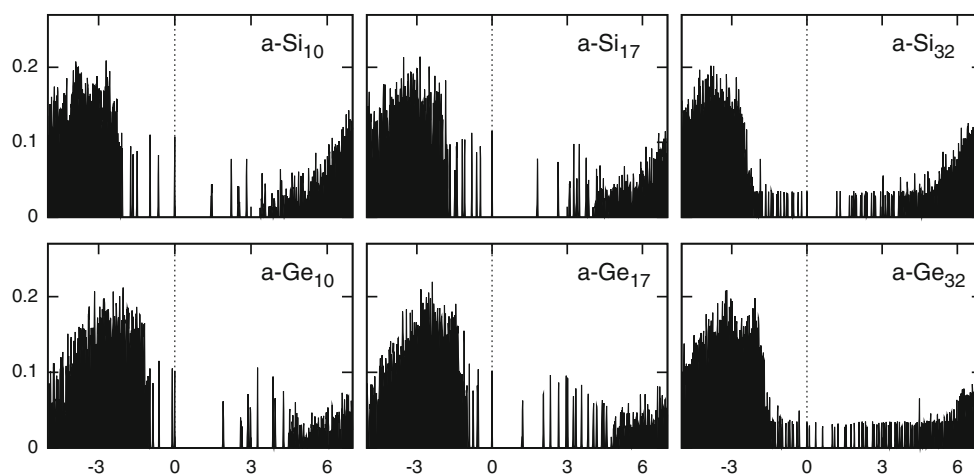
**Fig. 2** Normalized DOS for the amorphized pure Si and Ge NCs. Energy units are in eV. The *dotted lines* marks the HOMO state that has been positioned at 0 eV
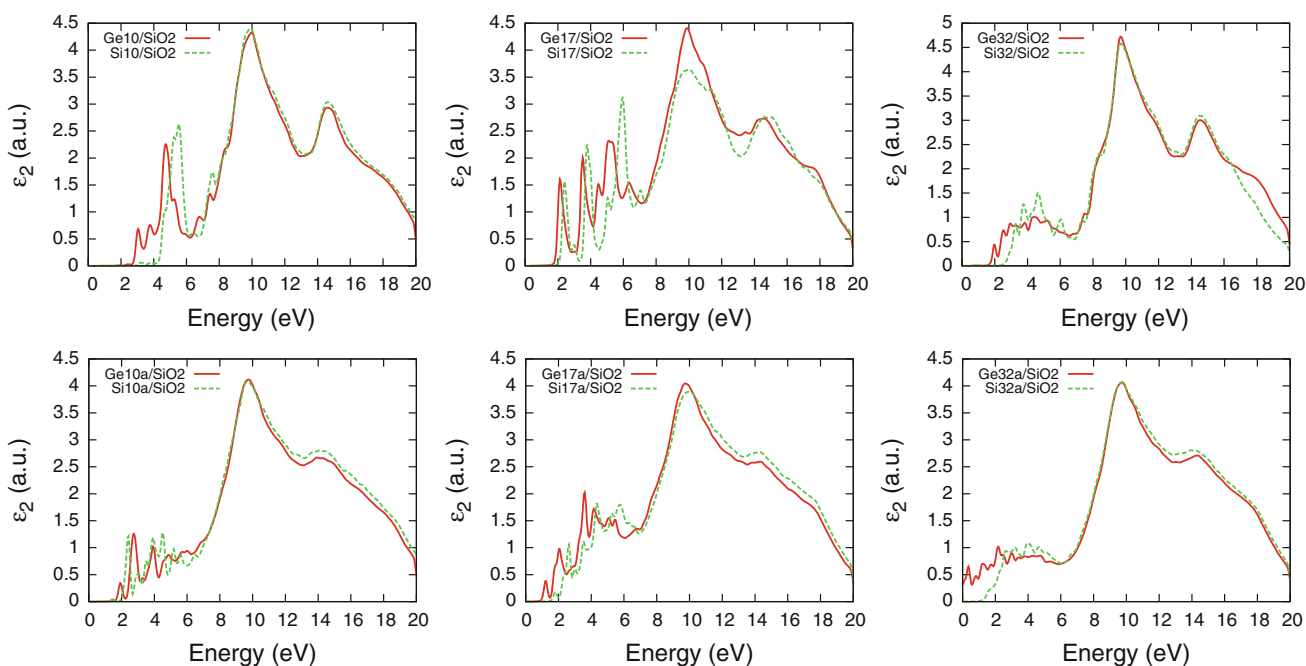


**Fig. 3** Imaginary part of the dielectric function for the crystalline (*top*) and amorphous (*bottom*) embedded NCs, made by 10 (*left*), 17 (*center*), and 32 (*right*) atoms, respectively. For each plot a comparison of the responses of Si (*dashed*) and Ge (*solid*) NCs is provided (color online)

energy for which the absorption is greater than 2.5% of the highest peak (corresponding to about 0.1 a.u.); in this way, we introduce a sort of "instrument resolution" that neglects very unfavorable optical transitions (for instance the 2–4 eV spectral region of the $Si_{10}/SiO_2$ crystalline system). The absorption thresholds show a trend that generally decrease with the NC size, highlighting the fundamental role of QC at this stage. The amorphyzation tends to smooth-out the curves and to reduce the absorption threshold of about 1 eV. Also, all the Ge-NCs present lower thresholds with respect to their Si counterparts.

Therefore, by varying the composition and the disorder of a NC of fixed size, we can obtain impressive variations of the absorption threshold up to about 2.7 eV.

This result can motivate the employment of Ge together with Si for the production of semiconductor-based NCs, in order to improve the possibility of tuning the opto-electronic response by selecting, in addition to the structural configuration, also the composition of the NC. Another opportunity comes from the exploitation of alloyed Si/Ge-NCs, that could provide additional control over the final response as discussed in the next section.
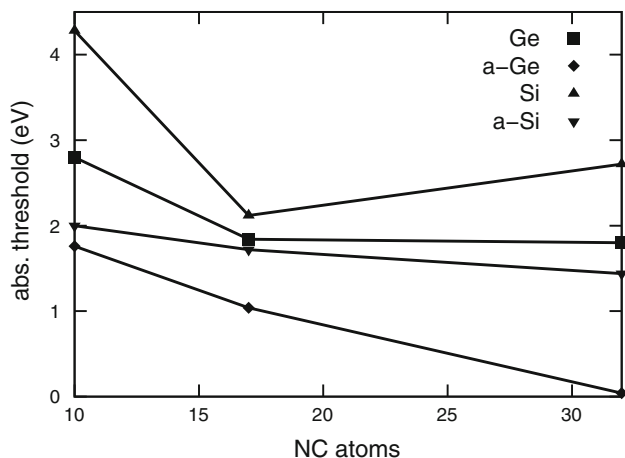
Fig. 4 Absorption thresholds for the pure Si and Ge NCs (see text). The *lines* are drawn to guide the eye



Fig. 6 Imaginary part of the dielectric function calculated in RPA for the $Si_{32}$ (*dashed*), $Ge_{16}Si_{16}$ (*dotted*), and $Ge_{32}$ (*solid*) crystalline embedded NCs. *Inset* absorption threshold as a function of the alloy index, $x$ (color online)

## Alloyed Si/Ge Nanocrystals

In this section, we consider the case of the $Ge_{16}Si_{16}$ NC, that has been built starting from the pure $Si_{32}$ NC by replacing half of the NC with Ge atoms and then by totally relaxing the resulting alloyed. The crystallinity of the system permits a net specularity in the geometry of the two halves of the compound. This choice eliminates any complication that may arise from differences in the structural configuration of the two halves, eventually overbalancing the response of one species with respect to the other.

By comparing the responses of the pure Si and Ge systems with that of the alloy, we investigate the effects of the alloying on the electronic configuration and on the absorption spectrum. In Fig. 5, we report the DOS projected (PDOS) on the atoms belonging to the NC, for the pure and the alloyed NCs. For all the cases, the PDOS concentrates near the band edge while getting weaker for energies lower than HOMO or higher than LUMO, in agreement with the fact that low-energy transitions mostly derive from states localized on the NC [24]. Some difference emerges between the PDOS of $Si_{32}$ and $Ge_{32}$ NCs, in particular near the valence band edge, where the former PDOS presents a higher concentration of states in the 0–1 eV energy range. Besides, the PDOS of the alloyed NC appears as a half-half mixture of the PDOS of the two pure NCs. Therefore, neither of the two species of the alloyed

NC seems to dominate over the other, with the final response of the alloyed system lying in-between those of the pure systems. The absorption spectra of the three samples (see Fig. 6) supports this argument, showing the curve of the $Ge_{16}Si_{16}/SiO_2$ NC nicely amongst the curves of the pure systems. Also the trend of the absorption threshold (see inset of Fig. 6) shows an-almost linear dependency with the alloy index, in nice agreement with the discussion earlier.

In order to explore deeper on the role of the alloying, we compare the charge localization of the HOMO and LUMO states for the pure and alloyed 32-atoms NCs. Due to the $T_d$ symmetry of the initial systems, the HOMO state forms a degenerate triplet before the relaxation, and therefore, for a proper comparison of the band-edge states we have to consider the set of non-degenerate HOMO-2, HOMO-1, and HOMO states of the relaxed system, that origins from the same symmetry group. From now on we will refer to all these states as HOMO(3). In Fig. 7 we report the HOMO(3) and LUMO states for the $Si_{32}/SiO_2$ (top panel) $Ge_{16}Si_{16}/SiO_2$ (center panel), and $Ge_{32}/SiO_2$ (bottom panel) NCs. For the pure systems we observe a partial separation of the HOMO(3)-LUMO density charges, with the former localized mainly on one half of the NC and the latter mainly on the other half. Such a separation is probably due to the distortion of the NC after the relaxation, favoring the localization of the charge on the most strained



Fig. 5 Normalized projected DOS for the 32 atoms crystalline NC in the pure-Si (*left*), half-half alloy (*center*), and pure-Ge (*right*) phases
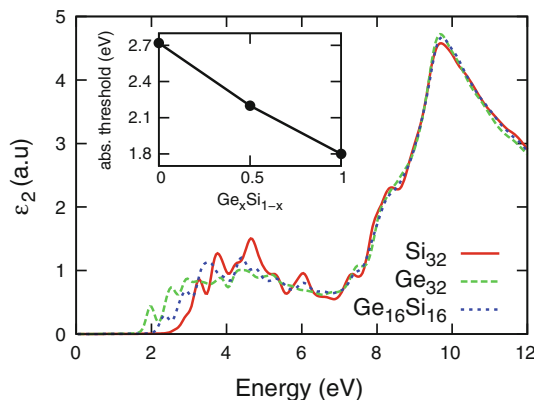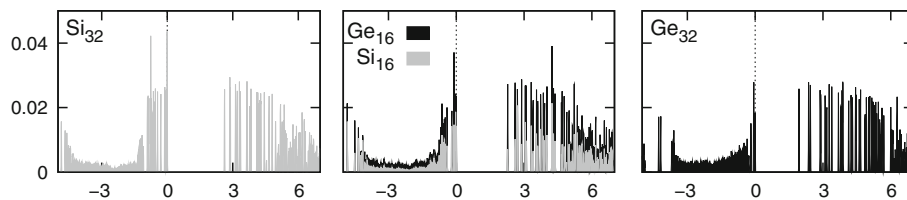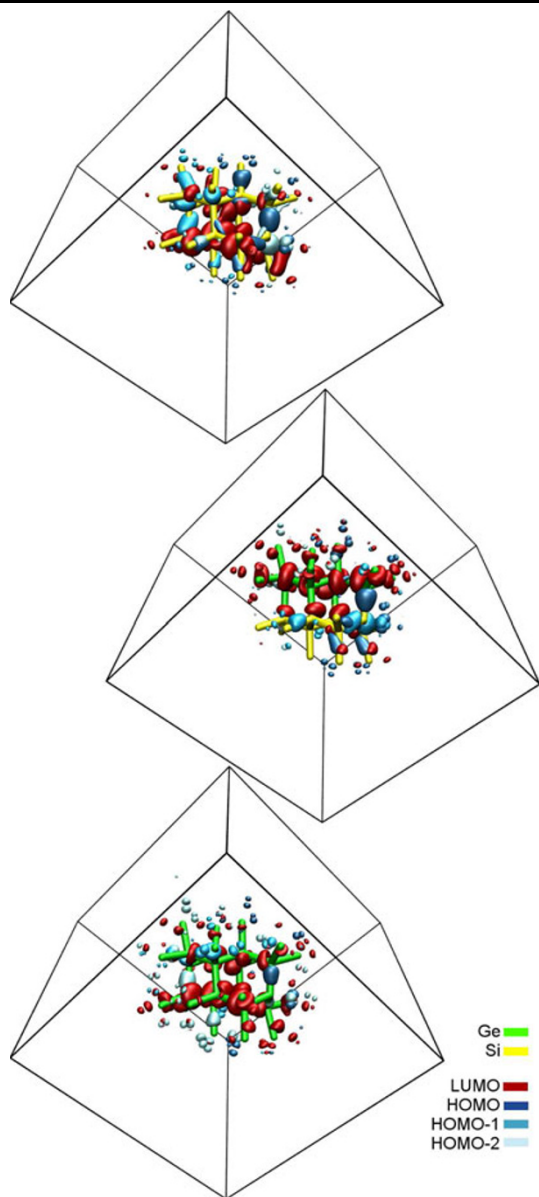
**Fig. 7** Kohn–Sham orbitals at 10% of their maximum amplitude for the $Si_{32}$ (*top*), $Ge_{16}Si_{16}$ (*center*), and $Ge_{32}$ (*bottom*) crystalline embedded NCs. The LUMO state is represented in *dark red* (*black*), the HOMO state is represented in *blue* (*gray*), the HOMO-1 in *azure* (*light gray*), and the HOMO-2 in *lightest blue* (*lightest gray*). The Si and Ge atoms of the NC are shown in *yellow* (*light gray*) and *green* (*gray*) thick sticks, respectively. For a better visibility of the images the $SiO_2$ atoms surrounding the NCs are not shown (color online)

bonds of the NC. In the case of the alloyed NC, the separation seems more pronounced, with the LUMO localized on the Ge atoms and the HOMO(3) on the Si atoms. It is not clear at this stage whether a real charge separation effectively occurs (as in the case of Si/Ge mixed nanowires, see section "Si/Ge Mixed Nanowires") or if such effect depends on the particular configuration of the NC considered here. More investigations are therefore required in order to shed some light on this important aspect.

## Si/Ge Mixed Nanowires

The scientific and technological importance of SiGe NWs is related to the peculiar physical properties that they present and that make them more suitable for PV with respect to the corresponding pure Si and Ge NWs. In fact it has been demonstrated, both experimentally and theoretically [12, 72–74], that the electronic and optical properties of SiGe NWs can be strongly modified by changing the size of the system (like in the pure nanowires [75–77]), but also by changing the relative composition of Si and Ge atoms and the geometry of Si/Ge interface [12, 78, 79]. This additional degree of control on the electronic structure makes these type of wires a possible route for PV because it offers a very wide range of possibilities to modulate the electronic structure of the material in order to obtain the desired properties. As discussed in section "Introduction", in order to improve the efficiency in PV it is necessary or to maximize the absorption spectrum, or to obtain inside the material, after the absorption of light, a strong separation of electron and hole, or to improve the rapidity of transfer electrons and holes to metallic electrodes. Here, we show how a particular type of SiGe NWs, called *Abrupt* SiGe NWs and characterized by a clear planar Si/Ge interface, can satisfy (more than the corresponding pure NWs) the requirements of a material for solar cell.

The free-standing NWs considered here are oriented along the [110] direction (that guarantees thermodynamic stability [80]) and have an approximately cylindrical shape; the diameter range is from 0.8 to 1.6 nm and all the surface atoms have been passivated with H atoms in order to eliminate the intra-gap states. For the details of the construction of the geometry of NWs we refer to Ref.[12, 78]. We have analyzed pure Si, pure Ge and *Abrupt* SiGe NWs. This particular type of SiGe NWs is characterized by the presence of a planar Si/Ge interface along the shortest dimension of the transverse cross-section of the wire [12, 78]. The compositional range for *Abrupt* SiGe NWs is $0 \leq x \leq 1$, where $x$ is the relative composition of one type of atom with respect to the total number of atoms in the unit cell. An energy cutoff of 30 Ry, a Monkhorst-Pack grid of $16 \times 1 \times 1$ points and 10 Å of vacuum between NWs replicas have been evaluated enough to ensure the convergence of all the calculated properties. In order to obtain the geometry of minimum energy of our structures, we have performed total energy minimization of the positions of atoms in the plane normal to the growth direction; while to take into account the effect of the strain in the direction of growth, we have used the Vegard's law for semiconductor bulk alloys [81], which very recently has been demonstrated also valid for nanoalloys and which states that the relaxed lattice parameter of a binary system is a linear function of the composition of the system. After

the evaluation of DFT-LDA ground state properties, in order to calculate the optical properties of the wires, in particular the excitonic wave function localization, we have solved the Bethe–Salpeter equation (BSE) in the basis set of quasi-electron and quasi-holes states, as described in section "Ab-initio Methods: DFT and MBPT".

As first step, we have estimated how the variation of the size of the system has an influence on the electronic DFT-LDA band gap of the wires; to analyze this aspect, we have fixed the composition of *Abrupt* SiGe NWs ($x_{Ge} = 0.5$) and we have calculated the scaling of the electronic band gap as a function of the inverse of the diameter of the wire. Our results are reported in Fig. 8. Clearly, for all the types of NWs, on reducing the size of the wire (that means moving from left to right in Fig. 8) the electronic band gap increases; this result, as demonstrated in many theoretical and experimental works, is strictly related to the QC effect [16, 74–77, 82]. Moreover the most interesting result is that *Abrupt* SiGe NWs show a pronounced Reduced QC Effect (RQCE) [12, 78]: this means that, when the size of the system is reduced, the opening of the bulk band gap is not so strong like in the pure wires of similar size and therefore, at fixed diameter, the band gap of *Abrupt* SiGe NWs is smaller than the one of pure wires. Then we have analyzed how, at fixed diameter, the variation of composition for *Abrupt* SiGe NWs influences the electronic band gap. To do this, we have fixed the size of the wire and we added or deleted some rows of one type of atom in the transverse cross section (along the shortest dimension) of the wire in order to preserve a clear interface between Si and Ge (that is the main feature of this type of wire). In Table 4, we report the electronic DFT-LDA band gap $E_g$ as a function of the relative composition $x_{Ge}$ for *Abrupt* SiGe NWs with $d = 1.6$ nm (Fig. 9).
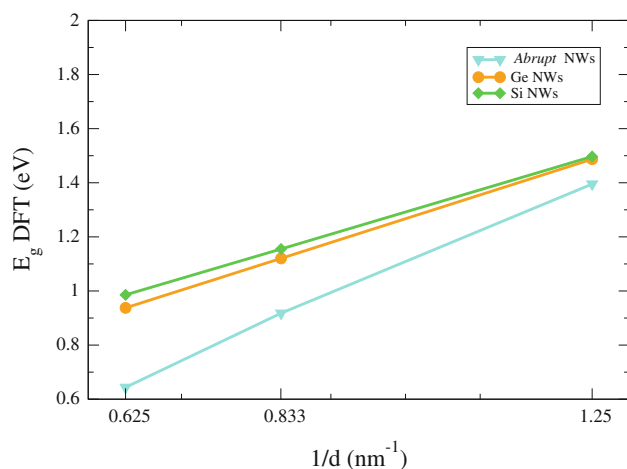
**Table 4** DFT-LDA electronic gaps (in eV) as function of Ge composition $x_{Ge}$ for *Abrupt* SiGe NWs with $d = 1.6$ nm

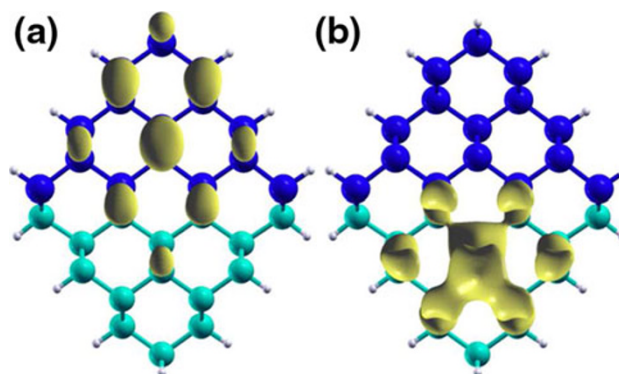| Composition $x_{Ge}$ | DFT-LDA $E_g$ |
|---|---|
| 1 | 0.9376 |
| 0.8958 | 0.9278 |
| 0.6875 | 0.6845 |
| 0.5000 | 0.6438 |
| 0.3125 | 0.6834 |
| 0.1042 | 0.8616 |
| 0 | 0.9856 |



**Fig. 9** Electronic wave function localization for VBM (**a**) and CBM (**b**) at Γ point for an *Abrupt* SiGe NW with diameter $d = 1.2$ nm and composition $x_{Ge} = 0.5$. *Blue spheres* represent Ge atoms, *cyan spheres* represent Si atoms, while *white spheres* are H atoms used to saturate the dangling bonds (color online)

By analyzing the numerical values, we can say that also the variation of the composition causes a reduction of the electronic band gap with respect to those of the pure wires. Therefore the composition, like as the diameter of the wire in the previous case, is responsible of a strong RQCE in this case. In particular $E_g$ depends on $x_{Ge}$ in a quadratic form [78]. This result represents a very useful tool in order to engine a material with the desired electronic properties and also in order to predict the absorption spectra of the wire. Since the RQCE is responsible for a red-shift in the absorption spectra of *Abrupt* SiGe NWs [83], it offers the possibility to access wavelengths that would otherwise not be available within a single material; this feature can be crucial for the engineering of a solar cell. The physical origin of the pronounced RQCE can be ascribed to the existence of type II band offset, when there is a planar interface between the two semiconductors. This type of offset implies that the minimum of conduction band (CBM) and the maximum of the valence band (VBM) are localized on different materials. In the next figure, we show how, for the *Abrupt* SiGe NWs, the wave function spatial localization is very strong, in particular the VBM is localized on the Ge part of the wire, while the CBM is



**Fig. 8** DFT-LDA bandgap as a function of the inverse of the diameter of the wire for Si NWs (*green line*), Ge NWs (*orange line*) and for *Abrupt* SiGe NWs with $x_{Ge} = 0.5$ (*cyan line*) (color online)

localized on the Si part of the wire. This property is also present, if we change the diameter or the composition of the system [78]. The type II offset is still present when the composition of the wire is varied, because, during the variation, we preserve the planar interface between Si and Ge, that offers a strong degree of control on the carriers space localization. As a confirmation of this idea, we have evaluated, through MBPT [84], the spatial localization of the lowest exciton of an *Abrupt* SiGe NW, with $d = 1.6$ nm and with $x_{Ge} = 0.6875$ (see Fig. 10). Fixing the position of the hole in the Ge part of the wire, one can note that the electronic probability distribution function is mainly localized on the Si part of the wire. This property is a demonstration of a clear tendency for these type of systems to strongly separate electrons and holes, a property useful in PV applications, offering a strong degree of control on the carriers localization.

Finally, we present one example of the electronic band structure for the *Abrupt* SiGe NWs. In Fig. 11, the one-dimensional band structure along the wire axis of an *Abrupt* SiGe NW with $d = 1.2$ nm and composition $x_{Ge} = 0.5$ is reported. The most interesting result is that the band structure shows a direct gap at the $\Gamma$ point; this property, as already demonstrated for pure Si and pure Ge wires with the same spatial orientation [16, 32, 60, 85], derives from the folding of the bulk energy bands onto the wire axis. Since the electronic wave function for the CBM at $\Gamma$ point is
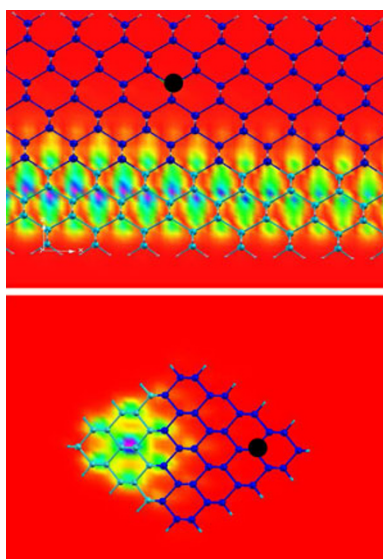


**Fig. 10** *Side* (*top panel*) and *top* (*bottom panel*) view of the electron distribution probability when the hole position is fixed on *top* of the Ge atom indicated by a *black dot*. The wire under consideration is an *Abrupt* SiGe NW with diameter $d = 1.6$ nm and composition $x_{Ge} = 0.6875$. *Blue spheres* represent Ge atoms, *cyan spheres* Si atoms, while the small *white spheres* are H atoms used to saturate the dangling bonds. The isosurface of the e-h distribution probability is shown in *green-yellow* (color online)
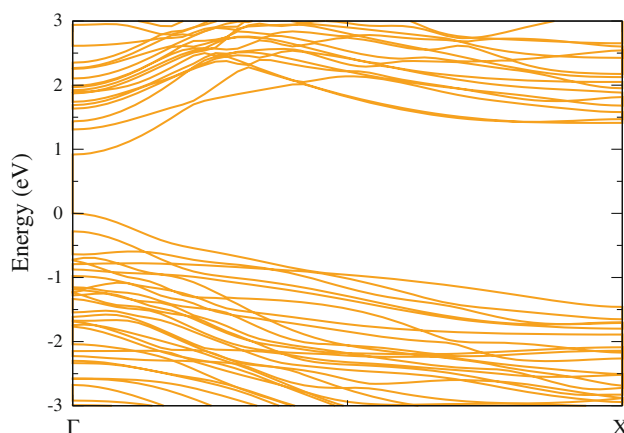


**Fig. 11** Electronic band structure along the wire axis for an *Abrupt* SiGe NW with diameter $d = 1.2$ nm and composition $x_{Ge} = 0.5$ (color online)

completely localized on Si, one can conclude that the direct band gap comes out from the folding of one of the six equivalent valleys of the Si bulk band structure onto the $\Gamma$ point. Moreover it is important to point out that the indirect CBM (at X) is located more than 0.5 eV higher than the $\Gamma$ point CBM. The presence of a direct band gap can have remarkable consequences for the technological applications of these wires: in fact it can modify the optical properties of a device, since offers the possibility to have optical transitions without involving phonons, thus increasing the optical intensities. However, a direct band gap structure alone do not ensure that a particular nanostructure will have a strong optical transitions [86]. Therefore further calculations concerning optical properties are needed in order to completely characterize these materials.

## Conclusions

In this paper, we have presented ab-initio computational methods for determining the structural, electronic and optical properties of Si and Ge nanostructures. We have concentrated our interest to those nanostructures that play a role in PV applications. In particular, we presented one-particle and many-body results for Si and Ge nanocrystals embedded in oxide matrices and for mixed SiGe nanowires. The discussed results shed light on the importance of many-body effects in systems of reduced dimensionality. In particular, we showed for embedded Si and Ge nanoparticles how the absorption threshold depends on size and oxidation and we have calculated the exciton binding energies. Besides, we have elucidated the role of crystallinity and through the calculation of recombination rates and absorption properties we have highlighted the best conditions for technological applications. In the case of

Si/Ge embedded alloyed nanocrystals, we have shown the dependence of the absorption spectra on the alloying and the presence of a different localization for HOMO and LUMO. Regarding the SiGe nanowires, we demonstrated that those which show a clear interface between Si and Ge originate not only a reduced quantum confinement effect but display also a direct band gap and a natural separation between electron and hole, a property directly related to PV potentiality.

# References

1. D.M. Bagnall, M. Boreland, Energy Policy **36**, 4390 (2008)
2. W. Shockley, H. J. Queisser. J. Appl. Phys. **32**, 510 (1961)
3. M. Green, P.A. Basore, N. Chang, D. Clugston, R. Egan, R. Evans, D. Hogg, S. Jarnason, M. Keever, P. Lasswell, J. O'Sullivan, U. Schubert, A. Turner, S.R. Wenham, T. Young, Solar Energy Mater. Solar Cells **77**, 857 (2004)
4. M. Grätzel, Nature **414**, 338 (2001)
5. M.A. Green, Third Generation Photovoltaics: Advanced Solar Energy Conversion (Springer, Berlin, 2003)
6. M. Grätzel, J. Photochem. Photobiol. A Chem. **164**, 3 (2004)
7. G. Conibeer, M. Green, R. Corkish, Y. Cho, E.-C. Cho, C.-W. Jang, T. Fangsuwannarak, E. Pink, Y. Huang, T. Puzzer, T. Trupke, B. Richeards, A. Shalav, K.-L. Lin, Thin Solid Films **511–512**, 654 (2006)
8. B. Tian, X. Zheng, T.J. Kempa, Y. Fang, N. Yu, G. Yu, J. Huang, C. M. Lieber, Nature **449**, 885 (2007)
9. M.D. Kelzenberg, D.B. Turner-Evans, B.M. Kayes, M.A. Filler, M.C. Putnam, N.S. Lewis, H.A. Atwater, Nano Lett. **8**, 710 (2008)
10. E.C. Garnett, P. Yang, J. Am. Chem. Soc. **130**, 9224 (2008)
11. A. Nduwimana, R.N. Musin, A.M. Smith, X.-Q. Wang, Nano Lett. **8**, 3341 (2008)
12. M. Amato, M. Palumbo, S. Ossicini, Phys. Rev. B **79**, 201302(R) (2009)
13. L. Cao, J.S. White, J.-S. Park, J.A. Schuller, B.M. Clemes, M.L. Brongersma, Nature Mater. **8**, 643 (2009)
14. S. Ossicini, L. Pavesi, F. Priolo, Light Emitting Silicon for Microphotonics, Springer Tracts on Modern Physics, vol 194 (Springer, Berlin, 2003)
15. C. Delerue, M. Lannoo, Nanostructures. Theory and Modelling (Springer, Berlin, 2004)
16. R. Rurali, Rev. Mod. Phys. **82**, 427 (2010)
17. P. Hohenberg, W. Kohn, Phys. Rev. **136**, B864 (1964)
18. W. Kohn, L. J. Sham, Phys. Rev. **140**, A1113 (1965)
19. E.K.U. Gross, M.A.L. Marques, Ann. Rev. Phys. Chem. **55**, 427 (2005)
20. G. Onida, L. Reining, A. Rubio, Rev. Mod. Phys. **74** 601 (2002)
21. A. Seidl, A. Görlig, P. Vogl, J.A. Majewski, M. Levy, Phys. Rev. B **53** 3764 (1996)
22. M. Gruning, A. Marini, A. Rubio, Phys. Rev. B. **74** 161103(R) (2006)
23. P. Giannozzi, S. Baroni, N. Bonini, M. Calandra, R. Car, C. Cavazzoni, D. Ceresoli, G.L. Chiarotti, M. Cococcioni, I. Dabo, A. Dal Corso, S. de Gironcoli, S. Fabris, G. Fratesi, R. Gebauer, U. Gerstmann, C. Gougoussis, A. Kokalj, M. Lazzeri, L. Martin-Samos, N. Marzari, F. Mauri, R. Mazzarello, S. Paolini, A. Pasquarello, L. Paulatto, C. Sbraccia, S. Scandolo, G. Sclauzero, A.P. Seitsonen, A. Smogunov, P. Umari, R.M. Wentzcovitch, J. Phys. Condens. Matt. **21**, 395502 (2009)
24. R. Guerra, I. Marri, R. Magri, L. Martin-Samos, O. Pulci, E. Degoli, S. Ossicini, Phys. Rev. B **79**, 155320 (2009)
25. M. Palumbo, S. Ossicini, R. De Sole, Phys. Status Solidi B **247**, 2089 (2010)
26. L. Hedin, Phys. Rev **139** A796 (1965)
27. F. Aryasetiawan, O. Gunnarsson, Rep. Prog. Phys. **61** 237 (1998)
28. M.S. Hybertsen, S.G. Louie, Phys. Rev. B **35** 5585 (1987)
29. R.W. Godby, M. Schlüter, L. J. Sham, Phys. Rev. B **37** 10159 (1988)
30. A.G. Marinopoulos, L. Reining, A. Rubio, N. Vast, Phys. Rev. Lett. **91**, 046402 (2003)
31. C. Spataru, S. Ismail-Beigi, L.X. Benedict, S.G. Louie, Appl. Phys. A **78** 1129 (2004)
32. M. Bruno, M. Palumbo, A. Marini, R. Del Sole, S. Ossicini Phys. Rev. Lett. **98** 036807 (2007)
33. F. Bruneval, S. Botti, L.Reining, Phys. Rev. Lett. **94**, 219701 (2005)
34. B. Aradi, L.E. Ramos, P. Deak, Th. Köhler, F. Bechstedt, R.Q. Zhang, Th. Frauenheim, Phys. Rev. B **76**, 035305 (2007)
35. N. Wang, Z.K. Tang, G.D. Li, J.S. Chen, Nature **408**, 50 (2000)
36. D. Kovalev, Phys. Rev. Lett. **77**, 2089 (1996)
37. M. Cazzanelli, D. Kovalev, L.D. Negro, Z. Gaburro, L. Pavesi, Phys. Rev. Lett. **93** 207402 (2004)
38. H. Kageshima, K. Shiraishi, in *Proceedings of 23rd International Conference on Physics Semiconduction*, World Scientific, Singapore, 1996, ed. by M. Scheffler, R. Zimmermann, p. 903
39. M. Luppi, S. Ossicini, J. Appl. Phys. **94**, 2130 (2003)
40. M. Luppi, S. Ossicini, Phys. Rev. B **71**, 035340 (2005)
41. F. Djurabekova, K. Nordlund, Phys. Rev. B **77**, 115325 (2008)
42. N. Daldosso, M. Luppi, S. Ossicini, E. Degoli, R. Magri, G. Dalba, P. Fornasini, R. Grisenti, F. Rocca, L. Pavesi, S. Boninelli, F. Priolo, C. Spinella, F. Iacona, Phys. Rev. B **68**, 085327 (2003)
43. P. Ordejón, E. Artacho, J. M. Soler, Phys. Rev. B **53**, R10441 (1996)
44. J.M. Soler, E. Artacho, J.D. Gale, A. García, J. Junquera, P. Ordejón, D. Sánchez-Portal, J. Phys. Condens. Matt. **14**, 2745 (2002)
45. T. Watanabe, K. Tatsamura, I. Ohdomari, Appl. Surf. Sci. **237**, 125 (2004)
46. D.E. Yilmaz, C. Bulutay, T. Cagin, Phys. Rev. B **77**, 155306 (2008)
47. P. Kroll, H. J. Schulte, Phys. Stat. Sol. B **243** (2006)
48. D.E. Yilmaz, C. Bulutay, T. Cagin, Phys. Rev. B **77**, 155306 (2008)
49. L. Martin-Samos, Y. Limoge, J.-P. Crocombette, G. Roma, N. Richard, E. Anglada, E. Artacho Phys. Rev. B **71**, 014116 (2005) (we gratefully thanks Layla Martin-Samos for the contribution relative to the generation of the glass)
50. G. Hadjisavvas, P.C. Kelires, Physica E **38**, 99 (2007)
51. M. Ippolito, S. Meloni, L. Colombo, Appl. Phys. Lett. **93**, 153109 (2008)
52. http://www.bethe-salpeter.org
53. R. Guerra, E. Degoli, S. Ossicini, Phys. Rev. B **80**, 155332 (2009)

54. E. Degoli, R. Guerra, F. Iori, R. Magri, I. Marri, O. Pulci, O. Bisi, S. Ossicini, C. R. Physique **10**, 575 (2009)
55. R. Guerra, I. Marri, R, Magri, L. Martin-Samos, O. Pulci, E. Degoli, S. Ossicini, Superlatt. Microstruc. **46**, 246 (2009)
56. R. Guerra, S. Ossicini, Phys. Rev. B **81**, 245307 (2010)
57. R. Guerra, E. Degoli, M. Marsili, O. Pulci, S. Ossicini, Phys. Status Solidi B **247**, 2113 (2010)
58. E. Luppi, F. Iori, R. Magri, O. Pulci, R. Del Sole, S. Ossicini, E. Degoli, V. Olevano, Phys. Rev. B **75**, 033303 (2007)
59. F. Iori, E. Degoli, R. Magri, I. Marri, G. Cantele, D. Ninno, F. Trani, O. Pulci, S.Ossicini, Phys. Rev. B **76**, 085302 (2007)
60. M. Bruno, M. Palummo, A. Marini, R. Del Sole, V. Olevano, A. N. Kholod, S. Ossicini, Phys. Rev. B **72**, 153310 (2005)
61. C. Delerue, M. Lannoo, G. Allan, Phys. Rev. Lett. **84**, 2457 (2000)
62. L.E. Ramos, J. Paier, G. Kresse, F. Bechstedt, Phys. Rev. B **78**, 195423 (2008)
63. R. Guerra, PhD Thesis 2009, unpublished
64. J. Heitmann, F. Müller, L. Yi, M. Zacharias, D. Kovalev, F. Eichhorn, Phys. Rev. B **69**, 195309 (2004)
65. J. Linnros, N. Lalic, A. Galeckas, V. Grivickas, J. Appl. Phys. **86**, 6128 (1999)
66. M. Glover, A. Meldrum, Opt. Mater. **27**, 977 (2005)
67. T. Shimitsu-Iwayama, T. Hama, D.E. Hole, I.W. Boyd, Solid State Electron. **45**, 1487 (2001)
68. M. Schneibner, M. Yakes, A.S. Bracker, I.V. Ponomarev, M.F. Doty, C.S. Hellberg, L.J. Whitman, T.L. Reinecke, D. Gammon, Nature Phys. **4**, 291 (2008)
69. G. Allan, C. Delerue, Phys. Rev. B **75**, 195311 (2007)
70. R. Lockwood, A. Hryciw, A. Meldrum, Phys. Rev. Lett. **89**, 263112 (2006)
71. L. Dal Negro, M. Cazzanelli, L. Pavesi, S. Ossicini, D. Pacifici, G. Franzó, F. Priolo, Appl. Phys. Lett. **82**, 4636 (2003)
72. R. Musin, X. Wang, Phys. Rev. B **71**, 165308 (2006)
73. R. Musin, X. Wang, Phys. Rev. B **71**, 155318 (2005)
74. J. Yang, C. Jin, C. Kim, M. Jo, Nano Lett. **6**, 12, 2679 (2006)
75. M. Bruno, M. Palummo, R. Del Sole, S. Ossicini, Surf. Sci. **601**, 277 (2007)
76. S. Beckman, J. Han, J. Chelikowsky, Phys. Rev. B **74**, 165314 (2006)
77. X. Zhao, C.M. Wei, L. Yang, M.Y. Chou, Phys. Rev. Lett. **92**, 236805 (2004)
78. M. Amato, M. Palummo, S. Ossicini, Phys. Rev. B **80** 235333 (2009)
79. M. Amato, M. Palummo, S. Ossicini, Phys. Status Solidi B **247**, 2096 (2010)
80. Y. Wu, Y. Cui, L. Huynh, C.J. Barrelet, D.C. Bell, C.M. Lieber, Nano Lett. **4**, 433 (2004)
81. L. Vegard, Z. Phys. **5**, 17 (1921)
82. D.D.D. Ma, C.S. Lee, F.C.K. Au, S.Y. Tong, S.T. Lee, Science **299**, 1874 (2003)
83. M. Palummo. M. Amato, S. Ossicini, Phys. Rev. B (2010) (under review)
84. A. Marini, C. Hogan, M. Grüning, D. Varsano, Comput. Phys. Commun. **180**, 1392 (2009)
85. A.N. Kholod, V.L. Shaposhnikov, N. Sobolev, V.E. Borisenko, F.A. D'Avitaya, S. Ossicini, Phys. Rev. B **70**, 035317 (2004)
86. A.N. Kholod, A. Saul, J.D. Fuhr, V.E. Borisenko, F.A. D'Avitaya, Phys. Rev. B **62**, 12949 (2000)